Dependence of EHD instability of plasma/liquid interface on liquid conductivity

Maryam Bordbar, Kamal Hajisharifi, Hassan Mehdian, Ali Hasanbeigi, Eric Robert

Dependence of EHD instability of plasma/liquid interface on liquid conductivity

Cite as: Appl. Phys. Lett. **124**, 251601 (2024); doi: 10.1063/5.0208701
Submitted: 16 March 2024 · Accepted: 10 June 2024 ·
Published Online: 17 June 2024

Maryam Bordbar,[1] Kamal Hajisharifi,[1,a)] Hassan Mehdian,[1] Ali Hasanbeigi,[1] and Eric Robert[2]

AFFILIATIONS

[1]Department of Physics and Institute for Plasma Research, Kharazmi University, 49 Dr. Mofatteh Avenue, Tehran, Iran
[2]GREMI, UMR 7344, CNRS/Université d'Orléans, Orléans, France

[a)]**Author to whom correspondence should be addressed:** hajisharifi@khu.ac.ir and k.hajisharifi@gmail.com

ABSTRACT

Besides numerous experimental reports revealing the characteristic dependence of depression on liquid surfaces induced by impinging plasma beams, and despite its scientific and practical importance, the physical mechanism responsible for this dependency has been missed. In this study, based on the border electrons' role, the water/plasma interfacial dynamics relevant to electrohydrodynamic instability (EHD) have been theoretically modeled, focusing on the characteristic dependence of the EHD growth rate driven by charge mobility mechanisms. The predictions of the growth rates dependent on water conductivity from theory agree well with our observations of faster plasma-filled underwater bubble explosions under lower conductivity conditions, indicating that the model contains the essence of the underlying physics of liquid surface deformation in the presence of plasma.

The interaction between plasma and liquid water has emerged as a promising technology for water purification,[1–3] wastewater treatment,[4–6] and disinfection applications.[7–9] Various methods are used to create an interface between the plasma and liquid media, including direct contact of plasma jets or sparks with the liquid surface, transporting afterglow plasma species into the liquid, injecting vapors or droplets into the gas phase, or generating plasma directly inside the gaseous bubbles. Studies have shown that plasma bubbles produce reactive species that degrade organic contaminants and inactivate microorganisms in water.[10–13] Experiments have shown that plasma factors (e.g., electron/ion density) and liquid conditions (e.g., temperature and conductivity) can be attributed to different outcomes, including bubble dynamics, interfacial area, plasma propagation distances, and chemical kinetics.[14–19] However, a complete physical understanding of the interaction between plasma and liquids to justify these attributions has not yet been achieved.[20,21] However, from a practical viewpoint, there is a pressing need to explain how linked plasma–liquid parameters affect the desired performance factors, such as treatment efficiency and the removal of specific pollutants.

Recently, the dependence of the plasma discharge process inside gas bubbles submerged in a liquid environment on liquid parameters has been experimentally reported.[22] A plasma gun (PG) device[23] was used to generate plasma inside gas bubbles immersed in the liquid. The plasma gun (PG) operates at 14 kV and 2 kHz pulse frequency, using a pure neon gas flow rate of 12–100 cm^3/ min. Owing to gas flow, bubbles formed at the tip of the PG. An intensified charge-coupled device (ICCD) camera was used along with the laser sensing of bubbles to image the plasma propagation inside the bubbles and study bubble dynamics. Figure 1 shows that starting from distilled water at time 0 and gradually shifting to a more conductive solution with the accumulation of the PG discharges, the bubble is less filled with plasma. In other words, bubbles in low-conductivity distilled water exhibit plasma that expands over the entire volume of the bubble with brighter emission, owing to electron accumulation at the bubble–liquid boundaries.[24,25] An interesting outcome of the experiments revealed a faster burst of plasma-filled bubbles in distilled water than in higher conductivity water, resulting in more rapid and homogeneous dispersal of the reactive species into bulk distilled water than into tap water. Previous experiments have suggested that instabilities at the gas bubble–liquid interface play a significant role in dissipating energy and causing rapid collapse of explosive gas bubbles immersed in liquids.[26]

In the present work, the theoretical model is generally used to determine the dependence of plasma–liquid surface deformation due to interfacial instabilities,[27–29] induced by charge accumulation around the surface, on liquid characteristics, especially water conductivity. To examine this claim, we present the simplified theoretical model to determine the conductivity dependence of the electrohydrodynamic (EHD) instability growth rate at the plasma–water interface. Our model offers physical insight by capturing perturbations at the

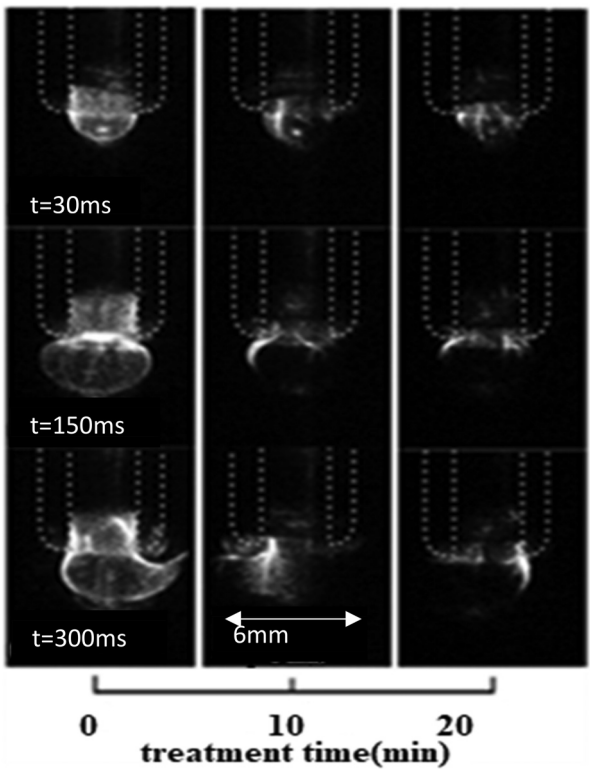

FIG. 1. Time resolved (ICCD camera delays of 30, 150, and 300 ms with respect to the bubble formation) images of the neon plasma in bubbles initiated at time 0 in distilled water (left hand side images) and gradually shifting to a more and more conductive solution with plasma gun discharge accumulation during 10 (central images) and 30 min (right hand side images). The water solution conductivity was measured to be 4, 65, and 130 μS/cm at time 0, 10, and 20 min, respectively.

interface and providing quantitative predictions of their evolution rates under various liquid conditions. It should be mentioned that the proposed model can be applied to unravel the physical mechanisms of a wide range of plasma applications based on plasma–liquid interactions. To qualitatively estimate the validity of the theoretical results, considering that interfacial instability causes bubble explosions,[26] the explosion time of the plasma-filled bubble has been experimentally considered as a key parameter for determining the connection between the interfacial instability growth rate and the conductivity of the liquid. In this regard, a higher interfacial instability growth rate leads to faster bubble explosion. In the experimental setup, high-speed imaging using either an ICCD camera or high frame rate camera visualization to capture plasma emission pattern and bubble dynamics, respectively, is employed at frame rates of up to 100 000 fps. Complementary optical identification using imaging analysis has been used in the experimental setup to monitor charge accumulation at the plasma–liquid interface for solutions with different conductivities. Analysis of the image data provided a qualitative evaluation of the bubble expansion rates, maximum diameter, surface deformation profiles, and critically, the explosion times as a function of the liquid electrical conductivity. The results clearly show that as the electrical conductivity of the liquid decreased, the bubble explosion time also decreased. This observed trend of faster bubble bursts in lower conductivity liquids agrees well with the theoretical model predictions, indicating higher EHD instability growth rates under such conditions. The strong correlation between our model's outputs and measurements underlines the crucial role of liquid properties on interfacial instability, which determines the bubble collapse intensity.

In this work, the plasma-filled bubbles generated by the plasma gun discharges delivered in various water conductivity samples are schematically described as sketched in Fig. 2. To analyze the dynamics of the plasma–water interface system, we divided it into three regions. First, the quasi-neutral bulk plasma exhibits zero net charge density and null electric field magnitude, which are related to plasma expansion along the boundary surface of the gas bubble with the surrounding liquid. Second, the anode sheath region next to the interface with a net charge corresponds to a brighter emission region owing to electron accumulation at the bubble–liquid boundaries. Third, a water environment with various degrees of conductivity surrounds the bubble, where a voltage is applied as a boundary condition corresponding to a negative discharge. The system comprising the incompressible water region next to the anode sheath is governed by a Poisson equation $\nabla \cdot \boldsymbol{E}_l = \frac{\varepsilon_w}{\varepsilon_l} q_p$ and a continuity equation $\frac{\partial q_l}{\partial t} + \nabla \cdot \boldsymbol{J}_l = 0$, where the subscripts $l = p, w$ are for the anode sheath and liquid water, respectively. The momentum conservation and current density equations for the liquid water region are as follows:

$$\boldsymbol{J}_w = q_w(\boldsymbol{E}_w + \boldsymbol{v}_w), \tag{1}$$

$$\frac{1}{M^2}\frac{\partial \boldsymbol{v}_w}{\partial t} = \frac{1}{T}\nabla^2 \boldsymbol{v}_w + \frac{1}{U}\hat{\boldsymbol{z}} - \nabla P_w + q_w \boldsymbol{E}_w, \tag{2}$$

and drift-diffusion relation for the anode sheath region is[30]

$$\boldsymbol{J}_p = -D.\nabla q_p - \frac{\mu_p}{\mu_w} q_p \boldsymbol{E}_p, \tag{3}$$

where $\boldsymbol{v}$, q, $\boldsymbol{J}$, $\boldsymbol{E}$, P, ρ, μ, and ε are the velocity, space charge density, electric current density, electric field, thermal pressure, mass density, mobility, and permittivity of the corresponding medium, respectively. Note that in these equations the following unit parameters have been adopted: L_0 is a unit length defined by the distance of the high voltage electrode from the bottom of the bubble, V is the unit potential, V/L_0 is the unit electric field, $\varepsilon_w V/{L_0}^2$ is the unit space charge density,

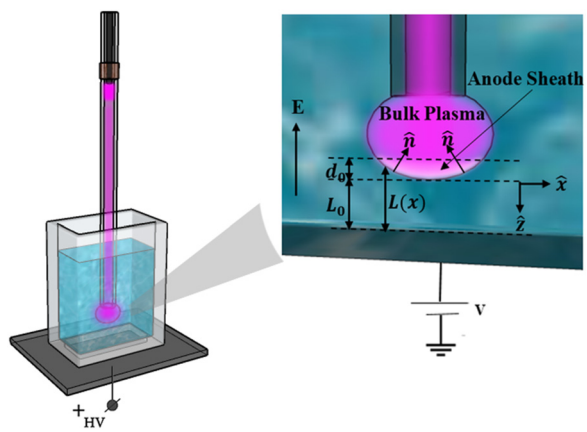

FIG. 2. Geometrical configuration of the system.

$\mu_w \varepsilon_w V^2/{L_0}^3$ is the unit current density, $\mu_w V/L_0$ is the unit velocity, ${L_0}^2/\mu_w V$ is the unit time, and $\varepsilon_w V^2/{L_0}^2$ is the unit pressure. The non-dimensional parameters appearing in above equations are $D = \frac{D_e}{\mu_w V}$, $T = \frac{\epsilon_w V}{\mu_w \eta}$, $M = \frac{1}{\mu_w}\sqrt{\frac{\epsilon_w}{\rho_m}}$, and $U = \frac{\epsilon_w V^2}{\rho_m g L_0^3}$, where η is the water dynamic viscosity, ρ_m is mass density of liquid water, g is gravitational acceleration, and $D_e = \frac{K_B T_e}{e}\mu_p$ is the diffusivity of the free electrons.

The aforementioned equations were solved numerically using appropriate boundary conditions to obtain the final solution. The boundary conditions for the upper edge of the anode sheath are $\phi_p = 0$ and $\partial\phi_p/\partial z = 0$, and for the lower edge of the water are $\phi_w = 1$, $q_w = \frac{Q L_0^2}{\epsilon_w V} \equiv c$ defined as the injection parameter, $v_w = 0$, and $v_w' = 0$. The electromechanical boundary conditions at the anode sheath–water interface are as follows:[31–33]

$$\boldsymbol{n} \times [\boldsymbol{E}] = 0, \tag{4}$$

$$-\frac{\partial f}{\partial t} + v_{zw} - v_{xw}\frac{\partial f}{\partial x} - v_{yw}\frac{\partial f}{\partial y} = 0, \tag{5}$$

$$\boldsymbol{n}.\left[\frac{\varepsilon_l}{\varepsilon_w}\boldsymbol{E}\right] = \sigma_s, \tag{6}$$

$$\frac{\partial \sigma_s}{\partial t} + v_n(\nabla \cdot \boldsymbol{n})\,\sigma_s + \boldsymbol{n}\cdot[\boldsymbol{J}] - [q\,\boldsymbol{v}]\cdot\boldsymbol{n} = 0, \tag{7}$$

$$\boldsymbol{t}\cdot\left[\frac{1}{T}(\nabla\boldsymbol{v} + \nabla\boldsymbol{v}^T)\right]\cdot\boldsymbol{n} + \sigma_s\cdot\boldsymbol{E}\cdot\boldsymbol{t} = 0, \tag{8}$$

$$\boldsymbol{n}\cdot\left[\frac{1}{T}(\nabla\boldsymbol{v} + \nabla\boldsymbol{v}^T)\right]\cdot\boldsymbol{n} - [P] - \left[\frac{1}{2}\frac{\epsilon_l}{\epsilon_w}\boldsymbol{E}^2\right] + \left[\frac{\epsilon_l}{\epsilon_w}(\boldsymbol{n}\cdot\boldsymbol{E})^2\right] - \frac{1}{Bo}\nabla_s\cdot\boldsymbol{n} = 0, \tag{9}$$

where σ_s, $\mathbf{t}$, $\mathbf{n}$, and ∇_s represent the surface charge density, unit vector tangent to the surface, unit vector normal to the surface, and surface gradient operator, respectively. The non-dimensional Bond number is defined as $Bo = \frac{\epsilon_w V^2}{\gamma L_0}$, where γ is the surface tension coefficient. The liquid interface is a material expressed by the kinetic equation [Eq. (5)], defined by the function $z = f(x, y, t)$.

In steady state,[34] the plasma side of the interface develops an anode sheath that transports electrons from the quasi-neutral bulk plasma to the interface. This yields an excess of free electrons and depletion of positive ions in the sheath adjoining the water surface. For simplification, ignoring the initial surface charge density owing to the low conductivity of the liquid, the flows, and the surface tension forces caused by the bubble's surface curvature does not contribute to or influence the equilibrium configuration of the system. Hence, stability analysis can be localized by neglecting the dependence of the geometrical parameters on x. Nonetheless, the surface tension force affects the instability metrics, such as perturbation expansion rates and transmission of interfacial disturbances. Our model is capable of capturing these curvature impacts on stability to some degree, even without resolving detailed interfacial charge dynamics.

By applying Poisson's equation at the equilibrium condition, the electrostatic potential of the anode layer can be derived by expanding the free electron density profile $q_p(z)$ as a Taylor series about the localized $d = \frac{d_0}{L_0}$, which represents the non-dimensional central thickness of the anode sheath. This approach can be represented as follows:

$$\frac{d^2\phi_p}{dz^2} = -\varepsilon_r q_p(z) = -\varepsilon_r\left[q_{p0} + q_p'(-d)(z+d) + \frac{q_p''(-d)}{2}(z+d)^2 + \cdots\right], \tag{10}$$

here, q_{p0} is the dimensionless free electron density at $z = -d$, ε_r is the dielectric constant of liquid water, and the values of $q_p'(-d)$ and $q_p''(-d)$ at the $z = -d$ can be determined using the plasma drift-diffusion equation. In this regard, the electric field approaches zero at the interface of the quasi-neutral bulk plasma and the anode sheath, and it is assumed that the current density J_p is spatially uniform and is carried predominantly by electrons across the non-neutral layer.

Applying these constraints allows for the analytical derivation of the plasma potential profile across the sheath region using the boundary condition, where both the electric potential and electric field vanish in the bulk plasma and at the upper edge of the anode sheath. Taking the limit of a small J_p as well as examining z less than the plasma Debye length λ_D leads to a plasma potential near the interface with an approximately parabolic shape, $\phi_p(z) = -\frac{\varepsilon_r q_{p0}}{2}(z+d)^2$. The ability to reasonably substitute an assumed parabolic profile instead of precisely determining the anode sheath potential distributions allows the analysis to be simplified substantially.[35,36]

On the water side of the interface,[31–33] the static electric field and charge density can be determined using Poisson's and current density equations. The equations yield $E_w(z) = -(az+b)^{\frac{1}{2}}$ and $q_w(z) = -a(az+b)^{-\frac{1}{2}}/2$, where the integration constants a and b are dimensionless. To complete the electrostatic model in the strong injection limit, boundary conditions are applied, and equilibrium parameters are calculated. Using values for various plasmas and low-conductivity water ($\sim 4\,\mu$S/cm) as listed in Table I, the proposed

TABLE I. Important parameters of the numerical model.

Parameter	Value
External applied voltage (V)	1000 V
Water layer length ($\mathbf{L_0}$)	0.01 m
Water mass density ($\boldsymbol{\rho_m}$)	1000 kg m^{-3}
Water dynamic viscosity ($\boldsymbol{\eta}$)	0.001 kg m^{-1} s^{-1}
Surface tension coefficient ($\boldsymbol{\gamma}$)	0.073 N m^{-1}
Free electron density	Variable
Electron temperature ($\boldsymbol{T_e}$)	Variable
Free space permittivity ($\boldsymbol{\varepsilon_p}$)	8.85×10^{-12} C m^{-1} V^{-1}
Rest mass of electron ($\boldsymbol{m_e}$)	9.109×10^{-31} kg
Electron charge (e)	1.6×10^{-19} C
Boltzmann's constant ($\boldsymbol{K_B}$)	1.381×10^{-23} J K^{-1}
Liquid water permittivity ($\boldsymbol{\varepsilon_w}$)	10^{-8} Cm^{-1} V^{-1} (Refs. 37 and 38)
Liquid water mobility ($\boldsymbol{\mu_w}$)	1, 2, 3 m^2 V^{-1} s^{-1} (Refs. 37 and 38)
Neutral density ($\boldsymbol{n_n}$)	2.5×10^{25} m^{-3}
Electron–neutral collision frequency ($\boldsymbol{\nu_{en}}$)	$2.6 \times 10^{-16}\, n_n\, T_e^{1/2}$ s^{-1} (Ref. 39)
Electron mobility ($\boldsymbol{\mu_p}$)	$e/m_e\nu_{en}$ m^2 V^{-1} s^{-1} Ref. 39)
Electron diffusivity ($\boldsymbol{D_e}$)	$\mu_p K_B T_e/e$ m^2 s^{-1} (Ref. 39)

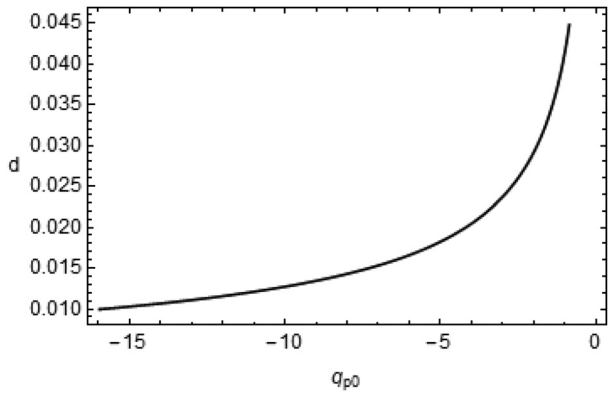

FIG. 3. The variation of dimensionless sheath thickness vs dimensionless electron density.

model results in a non-dimensional anode sheath thickness of approximately d = 0.01. As shown in Fig. 3, the anode sheath thickness decreases with increasing dimensionless electron density q_{p0}.

Figure 4 shows a set of plots depicting the structure of the interface under steady-state conditions between the anode sheath region on the left and adjacent liquid water on the right at $z = 0$. The black curves represent the normalized electric potential plotted against distance from the interface. The data points are connected smoothly at the boundary $z = 0$, indicating potential continuity. The density plots represent the electric field vs distance from the interface in each region. The electric field is somewhat larger at the anode sheath near the surface $(z = 0)$. This field accelerates electrons to the surface, because the sign remains negative all the way to the water anode surface. Owing to the discontinuity of the electric field at the interface $(z = 0)$, the electric field in water is approximately 1130 times smaller than that in the anode sheath (neglecting the surface charge), which corresponds to the dielectric constant of liquid water.[37,38] These results agree with the plotted charge density, as illustrated by the blue curves in the figure.

To investigate the instability of the plasma–water interface in the two-dimensional limit, we conducted perturbations of all quantities in the form $\psi(x, z, t) = \psi(z)\exp(ikx + \omega t)$. From this perspective, the perturbed surface can be expressed as $f(x, t) = f_0 \exp(ikx + \omega t)$, where ω is the growth rate of instability, and k is the perturbation wave number along the x-direction. To solve the perturbation problem effectively, it is convenient to have all equations defined in a common domain. This can be achieved by expressing the electric potential in the anode sheath gap as a new function, $g(z)$, defined in the interval $0 < z < 1$, where $\phi_{p1} = g(-d\,z)$.

In the next step, utilizing the static distributions of the electric field, electric potential, and charge density associated with each respective region as well as applying the relations described in Eqs. (1)–(3), the coupled differential equations can be formulated as follows:

$$g^{(4)} = \left(\frac{\omega}{D} - \frac{\mu_p q_{p0}}{D\,\mu_w}(1+\varepsilon_r)\right)\left(d^2 g'' - k^2 d^4 g\right) + 2k^2 d^2 g'' - d^4 k^4 g - \varepsilon_r \frac{\mu_p q_{p0}}{D\,\mu_w}(z+d)\left(-d\,g''' + k^2 d^3\,g'\right), \tag{11}$$

$$v_{1zw}^{(4)} = \frac{T\omega}{M^2}\left(v_{1zw}'' - k^4 v_{1zw}\right) + \left(2k^2 v_{1zw}'' - k^4 v_{1zw}\right) + k^2 T(az+b)^{\frac{1}{2}}\left(\phi_{1w}'' - k^2\phi_{1w}\right) + \frac{a^2}{4}\mathrm{T}k^2(az+b)^{-\frac{3}{2}}\phi_{1w}, \tag{12}$$

$$\phi_{1w}''' = \omega(az+b)^{-\frac{1}{2}}\left(\phi_{1w}'' - k^2\phi_{1w}\right) - \frac{a}{az+b}\left(\phi_{1w}'' - k^2\phi_{1w}\right) + k^2\phi_{1w}' + \frac{a^2}{4(az+b)^2}\left(\phi_{1w}' - v_{1zw}\right), \tag{13}$$

in which all quantities with subscript 1 denote the perturbation state. Therefore, the instability growth rate can be determined by solving the

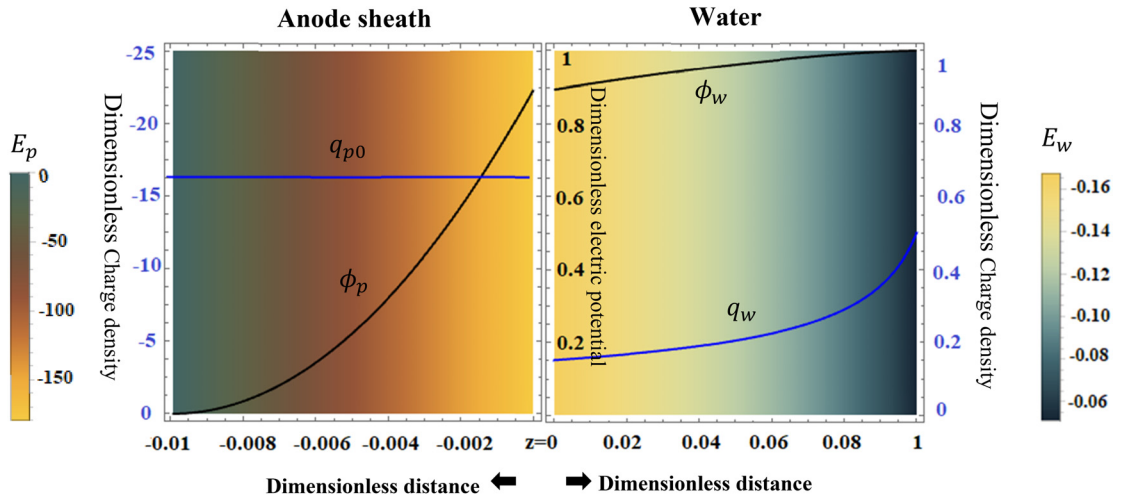

FIG. 4. Structure of the plasma–water interfacial region. Left: the anode sheath region near the water interface. Right: the water region. The black curves represent the electric potential and the blue curves represent the charge density profiles in each region. The mobility of liquid water is $\mu_w = 3\,\mathrm{m^2\,V^{-1}\,s^{-1}}$ and dimensionless electron density is $q_{p0} = -16$.

obtained equations simultaneously and applying the mentioned boundary conditions. Unlike the steady-state condition, one can note the incorporation of the effects of the surface tension forces $\nabla \cdot \boldsymbol{n}_1$ into the boundary formula in Eq. (9), which becomes particularly significant when distortion occurs. Finally, to numerically determine the conductivity-dependent growth rate of instability, we must solve an eleventh-order homogeneous system of ordinary differential equations with 12 boundary conditions. The formulated boundary value problem is approached by utilizing a boundary value problem solver available in MATLAB, namely bvp5c. The algorithm is particularly well suited for the computation of the dispersion relation $\omega(k)$, owing to the possibility of taking advantage of a continuation technique. This method uses the solution obtained for a given value of k as an initial estimate for the solution corresponding to the next value of k. This continuation technique is also useful for verifying the robustness of the solution. The solution computed with a given error tolerance (a parameter chosen by the user) is used as the initial guess for a new computation with a more stringent error tolerance. If the results remain stable, one can be confident about the obtained solution.

In Fig. 5, the dimensionless growth rate of instability is plotted against dimensionless perturbation wavenumber for various values of μ_w, T_e, and q_{p0}. Regarding the effect of the impinging electron temperature on the induced EHD instability, the electron temperature impacts the electron mobility μ_p through an inverse relationship with the electron–neutral collision frequency in the drift-diffusion equation [Eq. (3)] for the anode sheath current density. Enhancing the electron temperature increases the electron–neutral collision frequency, and thus decreases μ_p(see Table I). Therefore, one can expect that the growth rate of the instability decreases with increasing temperature owing to an increase in the collision frequency. In Fig. 5(a), the effect of electron temperature on the growth rate of instability is shown for $T_e = 1$ and 2 eV with fixed values of $\mu_w = 2\,\mathrm{m^2\,V^{-1}\,s^{-1}}$ and a dimensionless electron density of $q_{p0} = -16$. With plasma jet discharges at atmospheric pressure, the electron temperature variation is rather limited, the latter being most of the time around 1 eV, whatever the operating parameter for voltage peak amplitude, ranging from 1 to 20 kV. As can be seen in this figure, increasing the electron temperature slightly decreased the instability growth rate, as expected. In Fig. 5(b), the effect of electron density and liquid water mobility on the growth rate of instability is shown for $T_e = 1$ eV and different values of q_{p0} and μ_w. The solid lines correspond to a fixed value of the dimensionless electron density $q_{p0} = -16$, and the dashed lines correspond to a fixed value of the dimensionless electron density $q_{p0} = -11.2$. The curves show that the instability growth rate increases with decreasing liquid water mobility μ_w. Comparing the dashed and solid lines, it can be observed that by increasing the electron density or equivalently decreasing the anode layer thickness, the growth rate of the instability increases in all wavenumber ranges. This result shows that surface charge accumulation plays a critical role in the instability and deformation of plasma–liquid interfaces.[40] However, it is known that lower liquid conductivity and subsequently lower charge mobility[41] lead to greater charge accumulation around the interfacial region to produce stronger opposing electric fields, which counteract the externally applied field.[29,42] Therefore, increasing the instability growth rate by decreasing the liquid conductivity in Fig. 5 can be attributed to the enhanced charge accumulation around the surface. Physically, in agreement with our experimental results, as the conductivity of the liquid decreases, the mobility of dissolved ionic species responsible for charge transport correspondingly decreases, owing to a reduction in the ion population. The charge accumulated more readily around the liquid–plasma interface in the case of lower ion mobility, resulting in the generation of larger opposing electric fields that act against the externally applied field.[29,42] This enhances the stress exerted on the interface, which destabilizes the bubble surface through growing perturbations, leading to intensified instability. In fact, the lower charge mobility stemming from the lower solution conductivity is directly related to the exacerbated perturbation development and the subsequent interface deformation observed experimentally. Therefore, regulating the conductivity provides a means of manipulating the instability amplification by controlling the charge transport dynamics.

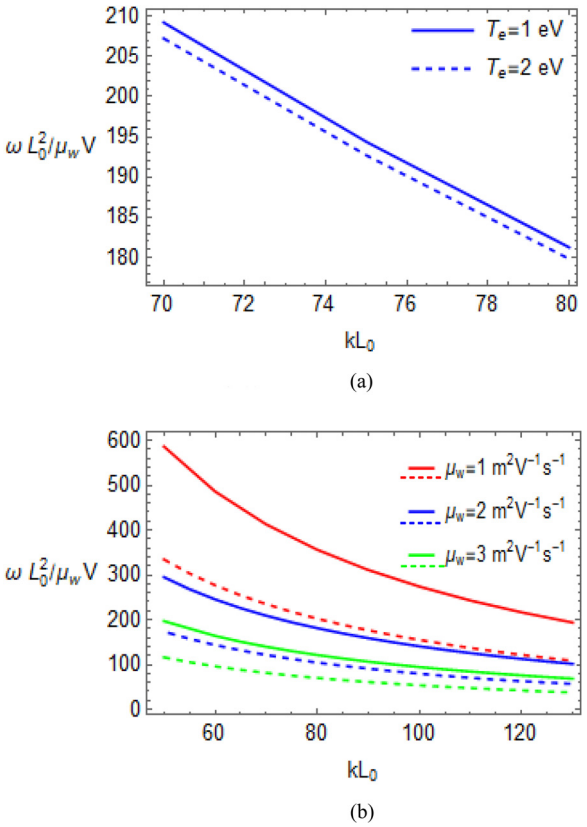

FIG. 5. (a) The dimensionless growth rate of instability with respect to the dimensionless wavenumber for $T_e = 1$ and 2 eV, with fixed values of $\mu_w = 2\,\mathrm{m^2\,V^{-1}\,s^{-1}}$ and $q_{p0} = -16$. (b) The dimensionless growth rate of instability with respect to the dimensionless wavenumber for $T_e = 1$ eV and different values of μ_w and q_{p0}. The solid lines represent the value of $q_{p0} = -16$, and the dashed lines represent the value of $q_{p0} = -11.2$.

In conclusion, the primary motivation behind creating a theoretical model to predict the instability growth rates at the plasma–liquid interface was to explain our observations of the experimental conductivity dependence of plasma-filled bubble deformation under a liquid. From a practical viewpoint, whether the controlled release of reactive agents for disinfection or the forceful collapse of bubbles for waste removal, an understanding of how the solution properties affect bubble

dynamics, like explosion time, could be of great importance. In this study, by quantitatively confirming the higher growth of perturbation for the lower conductivity case, the calculations validated the EHD interfacial instability as a major factor governing the asymmetric bubble shapes and their subsequent explosion. Attributing the conductivity effects to the perturbation of growth rates via charge mobility also elucidates the mechanisms that cause enhanced interface destabilization. Although a quantitative comparison between our experimental data and theoretical results is not feasible, the experimental data qualitatively align well with the theoretical predictions and meet our physical expectations. In this regard, while future refinements that disregard some assumptions used in the present work, higher order nonlinearities, or direct simulations may improve the quantitative accuracy, the current linear stability model, including some valid approximations, effectively explains the key mechanisms that govern the effects of conductivity on EHD instability growth rates, which is the central phenomenon of interest. The presented model framework can be utilized to determine the governing physics of various plasma applications based on plasma–water interactions through an analysis of the surface dynamics.

I gratefully acknowledge the input and friendship of many colleagues in shaping ideas in this present work and of many close associates, Professor Jean-Michel Pouvesle in particular.

AUTHOR DECLARATIONS

Conflict of Interest

The authors have no conflicts to disclose.

Author Contributions

Maryam Bordbar: Investigation (equal); Software (equal); Validation (equal); Writing – original draft (equal). **Kamal Hajisharifi:** Conceptualization (lead); Formal analysis (equal); Investigation (equal); Methodology (equal); Supervision (equal); Writing – original draft (equal); Writing – review & editing (equal). **Hassan Mehdian:** Conceptualization (equal); Investigation (equal); Supervision (equal); Writing – review & editing (equal). **Ali Hasanbeigi:** Formal analysis (equal); Software (equal); Visualization (equal); Writing – review & editing (equal). **Eric Robert:** Conceptualization (equal); Data curation (equal); Methodology (equal); Software (equal); Visualization (equal); Writing – review & editing (equal).

DATA AVAILABILITY

The data that support the findings of this study are available from the corresponding author upon reasonable request.

REFERENCES

[1]M. E. Shaer, M. Eldaly, and G. Heikal, Plasma Chem. Plasma Process. **40**, 971 (2020).
[2]P. Gururani, P. Bhatnagar, B. Bisht, V. Kumar, N. C. Joshi, M. S. Tomar, and B. Pathak, Environ. Sci. Pollut. Res. Int. **28**, 65062 (2021).
[3]D. Z. Yang, X. F. Zhou, J. P. Liang, Q. N. Xu, H. L. Wang, K. Yang, B. Wang, and W. C. Wang, J. Phys. D **54**, 244002 (2021).
[4]J. E. Foster, S. Mujovic, J. Groele, and I. M. Blankson, J. Phys. D **51**, 293001 (2018).
[5]J. E. Foster, Phys. Plasmas **24**, 055501 (2017).
[6]M. Magureanu, C. Bradu, D. Piroi, N. B. Mandache, and V. Parvulescu, Plasma Chem. Plasma Process. **33**, 51 (2013).
[7]D. C. Johnson, D. S. Dandy, and V. A. Shamamian, Water Res. **40**, 311 (2006).
[8]B. R. Locke, M. Sato, P. Sunka, M. R. Hoffmann, and J. S. Chang, Ind. Eng. Chem. Res. **45**, 882 (2006).
[9]J. Theron, J. A. Walker, and T. E. Cloete, Crit. Rev. Microbiol. **34**, 43 (2008).
[10]B. S. Sommers and J. E. Foster, Plasma Sources Sci. Technol. **23**, 015020 (2014).
[11]J. Foster, B. S. Sommers, S. N. Gucker, I. M. Blankson, and G. Adamovsky, IEEE Trans. Plasma Sci. **40**, 1311 (2012).
[12]R. Zhou, R. Zhou, P. Wang, P. W. B. Luan, X. Zhang, Z. Fang, Y. Xian, X. Lu, and K. K. Ostrikov, ACS Appl. Mater. Interfaces **11**, 20660 (2019).
[13]R. Andreozzi, V. Caprio, A. Insola, and R. Marotta, Catal. Today **53**, 51 (1999).
[14]P. Bruggeman P, C. Leys, and J. Vierendeels, J. Phys. D. **40**, 1937 (2007).
[15]A. Hamdan and M. S. Cha, J. Phys. D **48**, 405206 (2015).
[16]P. Bruggeman and C. Leys, J. Phys. D **42**, 053001 (2009).
[17]B. Jiang, J. Zheng, S. Qiu, M. Wu, Q. Zhang, Z. Yan, and Q. Xue, Chem. Eng. J. **236**, 348 (2014).
[18]J. Lai and J. E. Foster, J. Phys. D **53**, 025206 (2019).
[19]A. Hamdan, J. Profili, and M. S. Cha, Plasma Chem. Plasma Process. **40**, 169 (2020).
[20]A. Stancampiano, T. Gallingani, M. Gherardi, Z. Machala, P. Maguire, V. Colombo, J. M. Pouvesle, and E. Robert, Appl. Sci. **9**, 3861 (2019).
[21]P. J. Bruggeman, A. Bogaerts, J. M. Pouvesle, E. Robert, and E. J. Szili, J. Appl. Phys. **130**, 200401 (2021).
[22]A. Hamon, C. Douat, S. Dozias, J. M. Pouvesle, and E. Robert, in Proceeding of the 22nd International Conference on Gas Discharges and Their Applications, 2018.
[23]E. Robert, V. Sarron, T. Darny, D. Riès, S. Dozias, J. Fontane, L. Joly, and J. M. Pouvesle, Plasma Sources Sci. Technol. **23**, 12003 (2014).
[24]W. Tian, K. Tachibana, and M. J. Kushner, J. Phys. D **47**, 055202 (2014).
[25]K. Tachibana, Y. Takekata, Y. Mizumoto, H. Motomura, and M. Jinno, Plasma Sources Sci. Technol. **20**, 034005 (2011).
[26]S. Menon and M. Lal, Exp. Therm. Fluid Sci. **16**, 305–321 (1998).
[27]S. Park, W. Choe, H. Lee, J. Y. Park, J. Kim, S. Y. Moon, and U. Cvelbar, Nature. **592**, 49–53 (2021).
[28]X. Xue, L. Huang, Y. Yu, and Y. Liu, Phys. Plasmas **30**, 102103 (2023).
[29]A. Dickenson, J. L. Walsh, and M. I. Hasan, J. Appl. Phys. **129**, 213301 (2021).
[30]X Lu, GV Naidis, M Laroussi, and K Ostrikov, Phys. Rep. **540**, 123 (2014).
[31]A. Castellanos, A. I. Zhakin, P. K. Watson, P. Atten, and J. S. Chang, *Electrohydrodynamics* (Springer, Vienna, 1998).
[32]R. Chicon and A. T. Perez, Phys. Fluids **26**, 034103 (2014).
[33]R. Chicon and A. T. Perez, Phys. Fluids **18**, 104108 (2006).
[34]P. Rumbach, J. P. Clarke, and D. B. Go, Phys. Rev. E **95**, 053203 (2017).
[35]E. B. Tomme, D. A. Law, B. M. Annaratone, and J. E. Allen, Phys. Rev. Lett. **85**, 2518 (2000).
[36]K. Kano, *Semiconductor Devices* (Prentice Hall, Upper Saddle River, NJ, 1998).
[37]N. Zehtabiyan-Rezaie, M. Saffar-Avval, and K. Adamiak, J. Electrost. **96**, 151 (2018).
[38]N. Zehtabiyan-Rezaie, M. Saffar-Avval, and K. Adamiak, Desalination **497**, 114768 (2021).
[39]J. A. Bittencourt, *Fundamentals of Plasma Physics* (Springer, New York, 2004).
[40]L. Xiong, Z. Shu, Q, Huang, Q. Chen, X. Deng, X. Jiang, D. Wu, B. Bao, and Q. Xiong, Phys. Plasmas **26**, 063511 (2019).
[41]S. A. Norberg, W. Tian, E. Johnson, and M. J. Kushner, J. Phys. D **47**, 475203 (2014).
[42]S. A. Norberg, E. Johnsen, and M. J. Kushner, J. Appl. Phys. **118**, 013301 (2015).